Supplementary Information for:

Structure and DNA bridging activity of the essential Rec114–Mei4 trimer interface

Kaixian Liu, Emily M. Grasso, Stephen Pu, Shixin Liu, David Eliezer, and Scott Keeney

This pdf contains:

Supplementary Tables 1 and 2.
Supplementary Figures 1– 11

Additional information, in separate .avi files:

Supplementary Movies 1–5

Supplemental Table S1. Plasmids

Name	Description
pKL067	HisSUMO-Rec114(375-428):Mei4(1-43) in pETDuet1
pKL020	HisSUMO-Rec114(375-428):Mei4(1-43)-ybbR in pETDuet1
pSP63	HisSUMO-Rec114(325-428):Mei4(1-90) in pETDuet1
pKL080	Rec114(386-428):HisSUMO-Mei4(1-43) in pETDuet1
pKL086	Rec114(388-428):HisSUMO-Mei4(1-43) in pETDuet1
pKL077	Rec114(399-428):HisSUMO-Mei4(1-43) in pETDuet1
pKL088	Rec114(388-428):HisSUMO-Mei4(13-43) in pETDuet1
pKL110	HisSUMO-Rec114(375-428) in pSMT3
pKL075	mREC114(203-259):HisSUMO-mMEI4(1-42) in pETDuet1
pKL091	Rec114(388-428):HisSUMO-Mei4(1-43) Rec114 R394A/K395A in pETDuet1
pKL092	Rec114(388-428):HisSUMO-Mei4(1-43) Rec114 K399A/R400A in pETDuet1
pKL095	Rec114(388-428):HisSUMO-Mei4(1-43) Rec114 K417A/K424A in pETDuet1
pKL097	Rec114(388-428):HisSUMO-Mei4(1-43) Rec114 K403A/K407A in pETDuet1

Supplemental Table S2. Oligonucleotides

| Name	Sequence
KL020	AAAGATGTCCTAGCAATGTA
KL021	TACATTGCTAGGACATCTTT
KL024	CTAGTATAGAGCCGGCGCGCCATGTCTAGATAGCGTTAGGTCTGCCGAATAGTAC TACTCGGATCCCGAGCGAACCACGC
KL025	GCGTGGTTCGCTCGGGATCCGAGTAGTACTATTCGGCAGACCTAACGCTATCTAG ACATGGCGCGCCGGCTCTATACTAG
KL010	/5Cy3/ATTTCCACACCCTGTTTCTCCAGCGCAGCACCGTAAT
KL001	ATATCGCTGCCGGGCTGGGTGT
KL003	ATCTGGCTCGCCTGACGGGATGC
KL004	ATTTCCACACCCTGTTTCTCCAGCGCAGCACCGTAAT
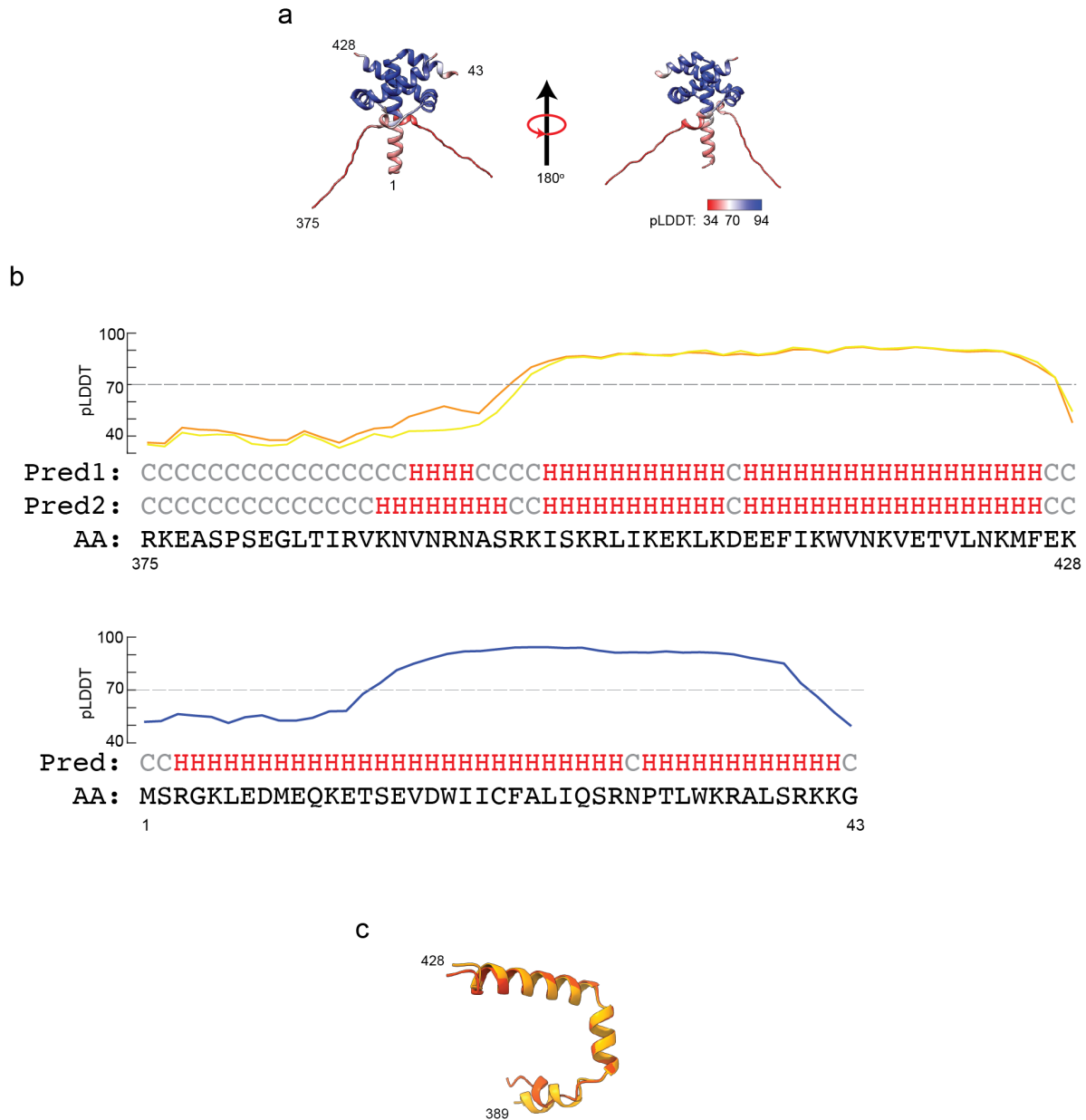
Fig. s1: AlphaFold2 model. (a) The AlphaFold2 model from **Fig. 1b** is color-coded by predicted local distance difference test (pLDDT) score. Residues with scores below 70 are considered low confidence. (**b**) Secondary structure prediction (Pred) and pLDDT score of the two Rec114$_C$ chains (top) and Mei4$_N$ (bottom) from the AlphaFold2 model. H: helix; C: coil. **(c)** Superimposition of α-helices 1–3 from the two copies of Rec114$_C$ in the AlphaFold2 model.
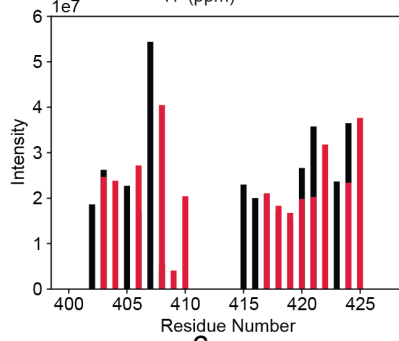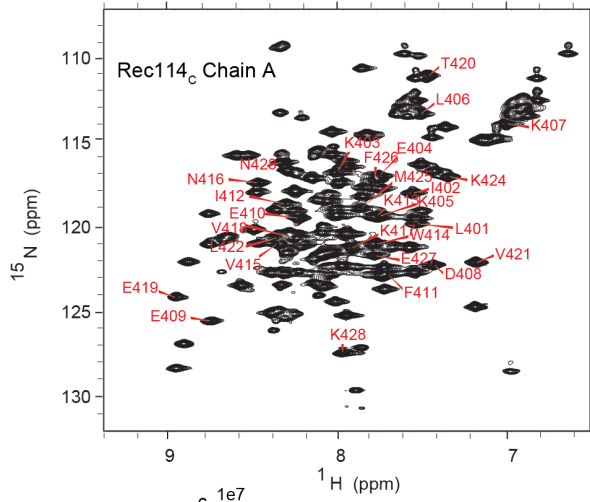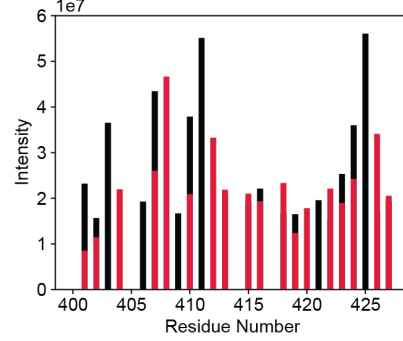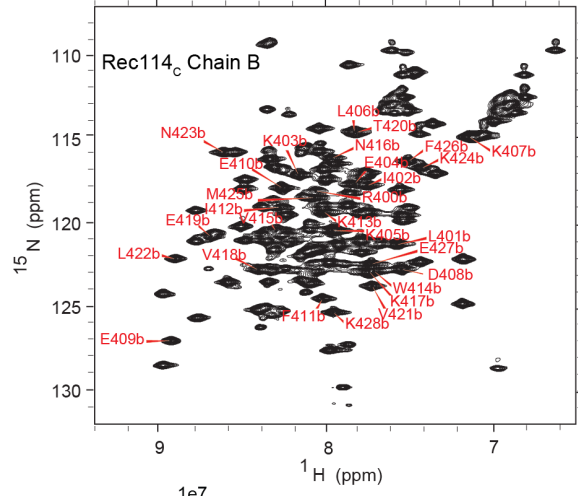
a

Rec114$_C$ Chain A

T420
L406
K407
K403 E404
F426
N423
M425 I402
K424
I412
K415 K405
E410
K411 W414 L401
V418
V422 E427
V415 D408
F411
E419
E409
K428

b

Rec114$_C$ Chain B

L406b
T420b
N423b K403b N416b F426b
F404b K424b K407b
E410b I402b
M425b R400b
E419b I412b K415b
V418b K413b K405b L401b
L422b E427b
D408b
W414b
K417b
F411b Y421b
E409b K428b

c

Mei4$_N$

S28
T32
K35
F23 R29 S39
G43
I21 T14 V17 L38
C22 Q27 W34
L25 Q20 Q11 M9 W19 R36
N30 I20 I26 D18
E16 K9
E13 A37
A24 R40
L6 D8 K12 L33
K41
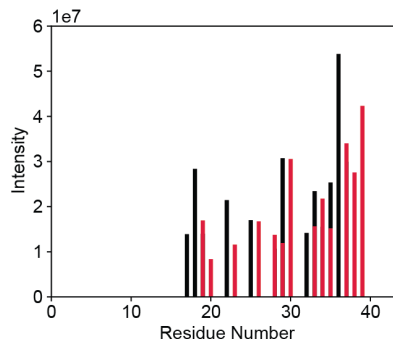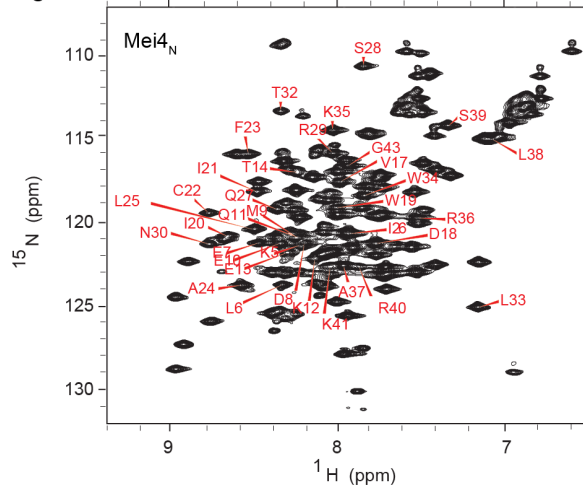
Fig. s2: Resonance assignments and NOEs for trimers of Rec114_C plus Mei4_N. (a, b) Top, assigned amide resonances for Rec114_C chains A and B, respectively. Note: we do not know which chain corresponds to which in the AlphaFold2 model. Bottom, i+1 (black) and i-1 (red) NH-NH NOEs for the assigned amides (residues 400–428) in each Rec114_C chain. **(c)** Top, assigned chemical shifts for Mei4_N. Bottom, NH-NH NOEs for the amides of residues 17–40 in Mei4_N.
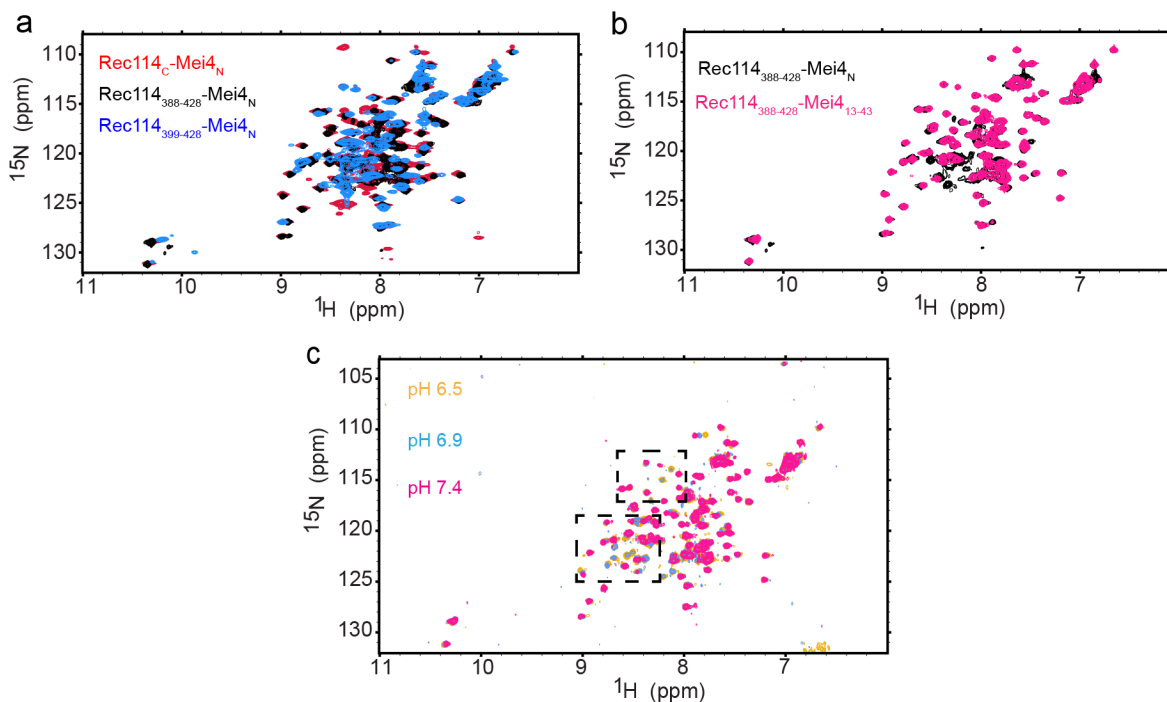
Fig. s3: NMR studies of truncated Rec114$_C$–Mei4$_N$ complexes at varying pH values. (a) Two-dimensional {^{1}H-^{15}N} HSQC spectra of complexes of Mei4$_N$ with Rec114 fragments Rec114$_C$ (red, 600 μM uniformly ^{15}N^{13}C-labeled protein collected at 800 MHz (^{1}H)), Rec114$_{388-428}$ (black, 45 μM uniformly ^{15}N-labeled protein collected at 500 MHz (^{1}H, Weill Cornell Medicine)), and Rec114$_{399-428}$ (blue, 500 μM uniformly ^{15}N^{13}C-labeled protein collected at 800 MHz (^{1}H)). Removing residues 375–387 resulted in minimal changes other than the elimination of peaks corresponding to the removed residues. In contrast, removing residues 375–398 resulted in significant chemical shift perturbations and line broadening, suggestive of partial unfolding and indicating that residues 388–398 are important for the stability of the complex. **(b)** Two-dimensional {^{1}H-^{15}N} HSQC spectra of complexes of Rec114$_{388-428}$ with Mei4$_N$ (black, 45 μM uniformly ^{15}N-labeled protein collected at 500 MHz (^{1}H, Weill Cornell Medicine)) or Mei4$_{13-43}$ (pink, 35 μM uniformly ^{15}N-labeled protein collected at 500 MHz (^{1}H, Weill Cornell Medicine)). Minimal differences were observed other than elimination of signals from the removed residues. **(c)** Two-dimensional {^{1}H-^{15}N} HSQC spectra of 30 μM of Rec114$_{388-428}$ and Mei4$_N$ at pH 7.4 (magenta), 6.9 (blue) and 6.5 (gold). Additional peaks, highlighted in dashed boxes, appear at the lower pH values. Samples with varied pH values were prepared in 25 mM NaHPO$_4$, 100 mM NaCl, 0.5 mM EDTA, 1 mM TCEP, 0.05% NaN$_3$, 5% D$_2$O. Spectra were collected at 25 °C at 500 MHz (^{1}H, Weill Cornell Medicine).
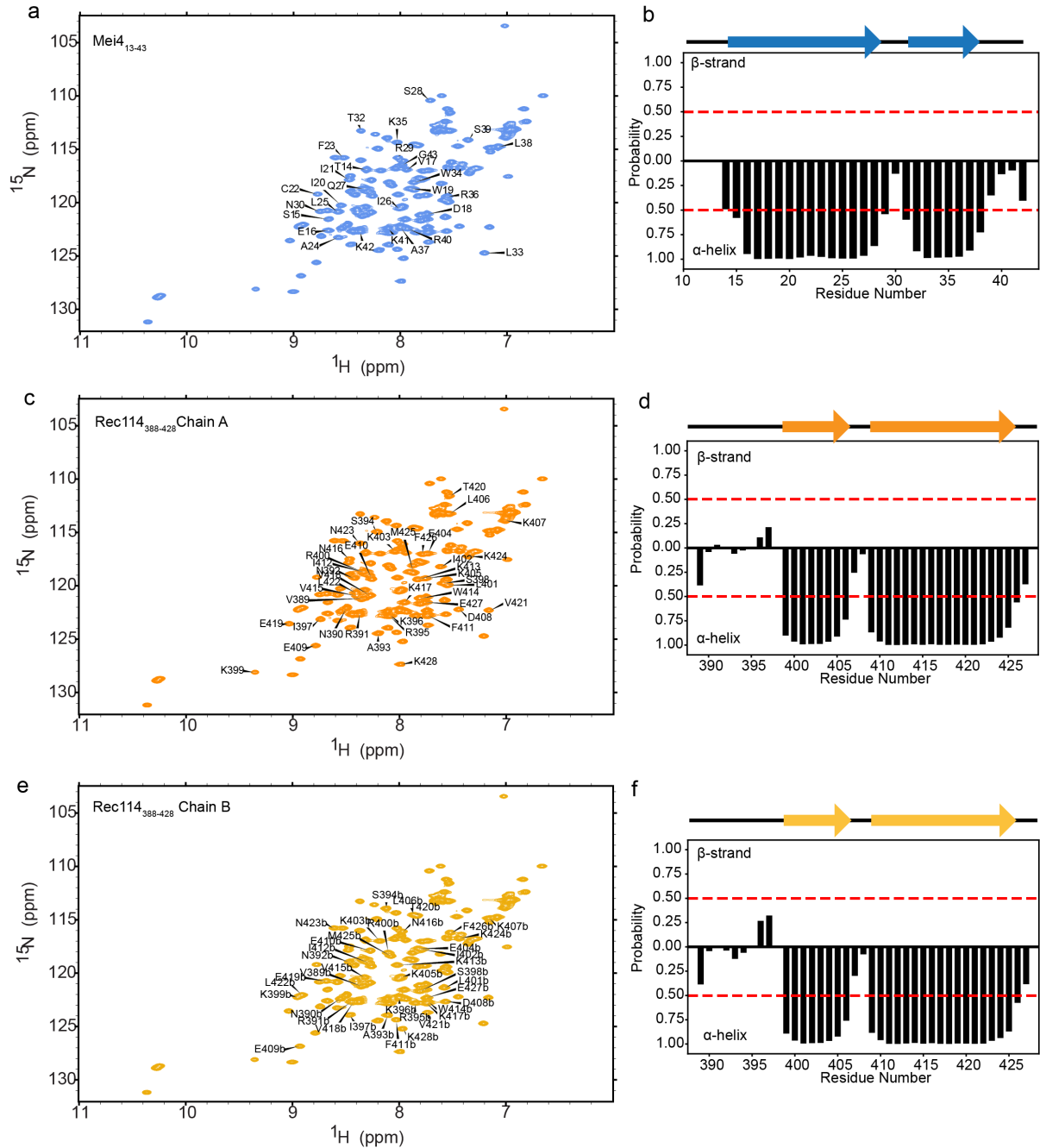
Fig. s4: NMR signals revealed at pH 6.1 indicate that the N-terminal region of Rec114$_C$ is not structured. (a, c, e) Assigned amide resonances for Mei4$_{13\text{-}43}$ (panel a) and the two Rec114$_{388\text{-}428}$ chains (panels c and e) within the Rec114$_{388\text{-}428}$–Mei4$_{13\text{-}43}$ complex. (**b, d, f**) TALOS-N secondary structure assessment for these residues. Stable helical structure was retained with the N-terminal truncation of Mei4. For both Rec114 chains, the previously seen helical structure was retained in this shorter construct, but the newly assigned residues 389–399 lack regular secondary structure.
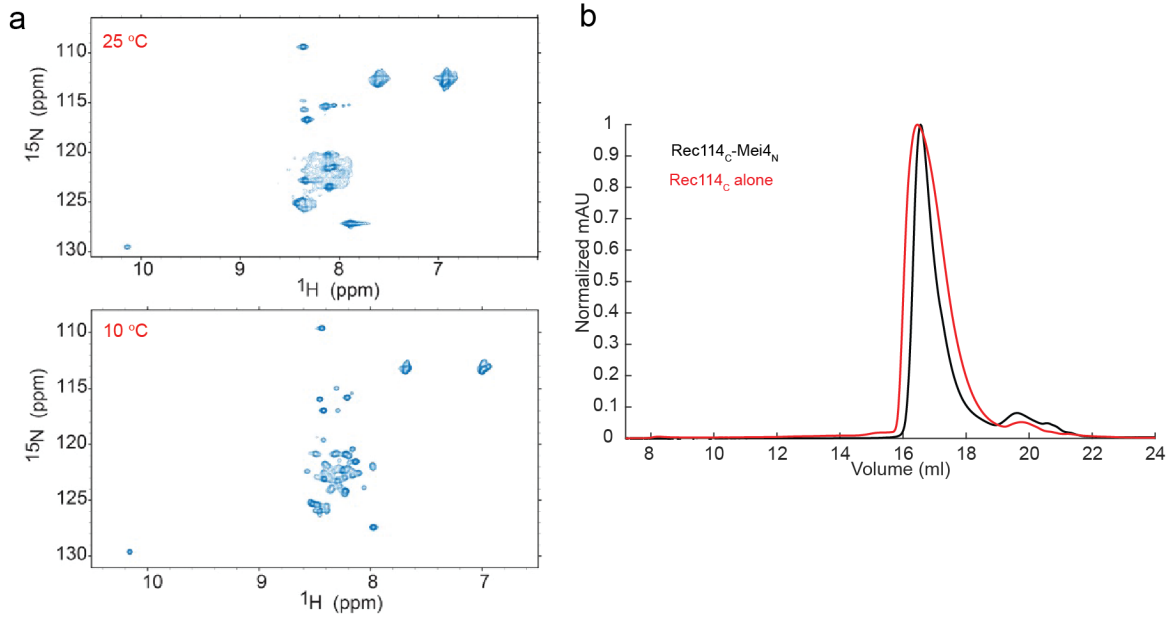
Fig. s5: Dimers of Rec114$_C$ alone are poorly structured. (a) Two-dimensional {^{1}H-^{15}N} HSQC spectra of Rec114$_C$ alone at 25 °C (top) and at 10 °C (bottom) show substantially less signal dispersion than for the trimeric complex, suggesting that Rec114$_C$ alone is substantially unfolded and/or aggregated. **(b)** Size exclusion chromatography comparing Rec114$_C$ alone with Rec114$_C$ plus Mei4$_N$.
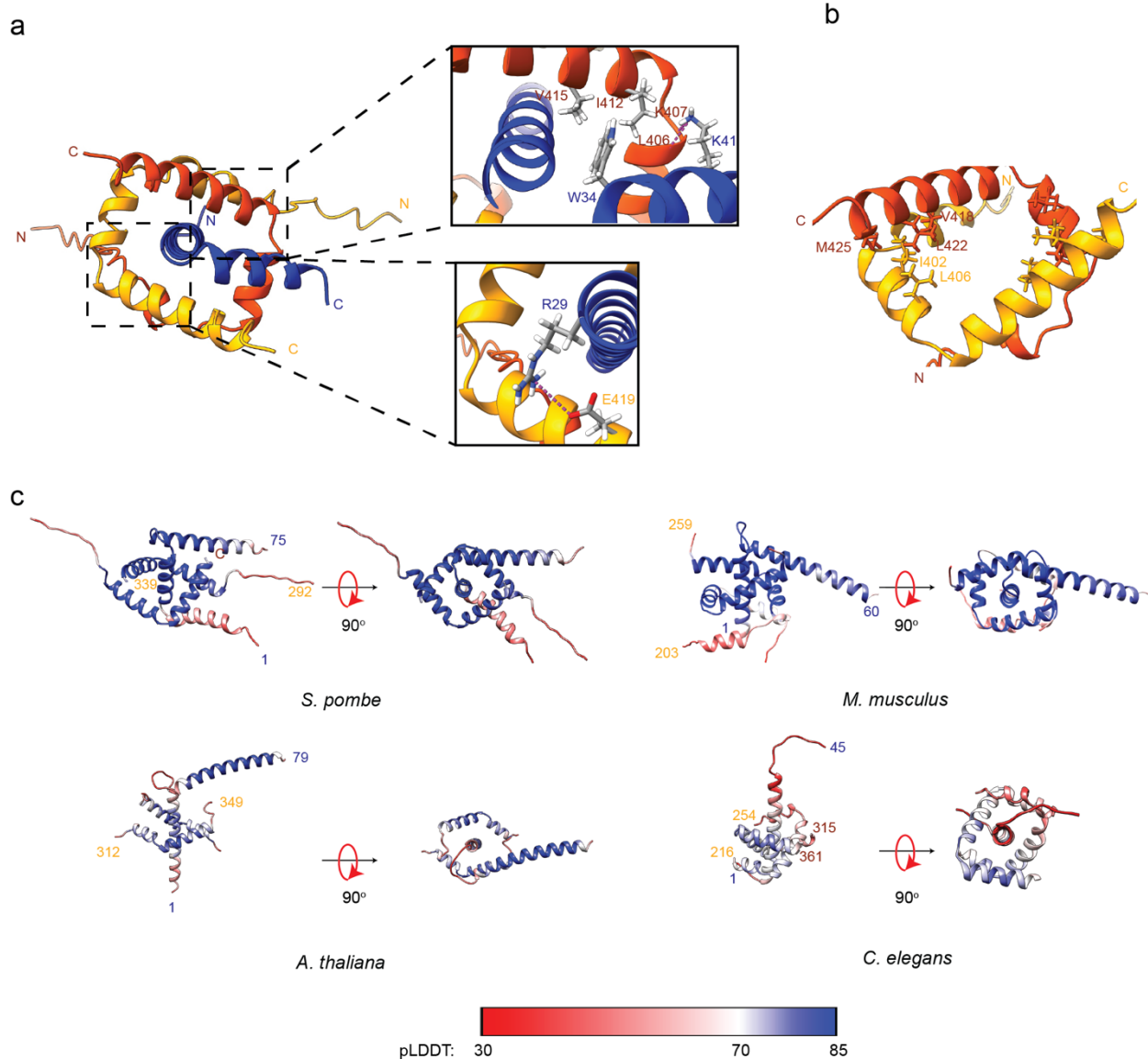
Fig. s6: Structure and conservation of Rec114–Mei4 interactions. (a) Asymmetric interactions between Mei4$_N$ and one chain of Rec114$_C$. The upper zoomed detail highlights hydrophobic contacts between W34 in Mei4 α-helix 2 and I412 and V415 in α-helix 3 from one copy of Rec114. Also shown are predicted hydrogen bonds between K41 in Mei4 α-helix 2 and the carbonyl oxygens of L406 and K407 from one copy of Rec114. The lower zoomed detail highlights a predicted salt bridge between Mei4 R29 and E419 from one copy of Rec114. **(b)** Hydrophobic interfaces between the two copies of Rec114. **(c)** AlphaFold2 models for orthologous Rec114$_C$–Mei4$_N$ complexes from the indicated species from **Fig. 3d**, color coded by pLDDT score. The starting and ending residue numbers are indicated.
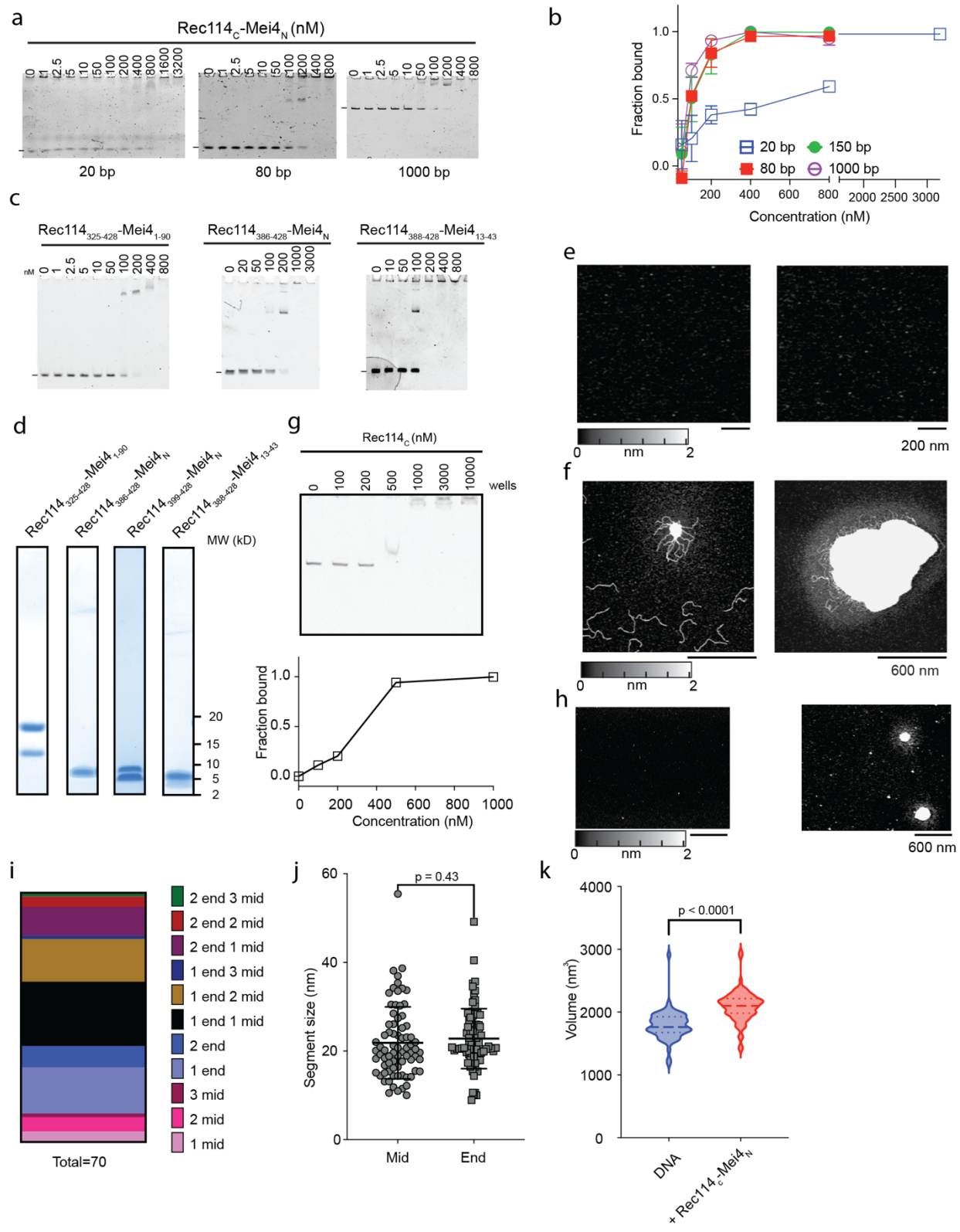
Fig. s7: DNA binding properties of the RM-TDB domain. (a, b) EMSAs testing binding of the RM-TDB domain to DNA substrates of varying lengths. Error bars indicate mean ± range (from two replicate experiments) or mean ± SD (from three replicates). Apparent affinities for the

different DNA lengths were: 20 bp, 600 ± 100 nM (N = 2 experiments); 80 bp, 100 ± 20 nM (N = 2); 150 bp, 90 ± 30 nM (N = 3, reproduced from **Fig. 4b**); 1000 bp, 80 ± 20 nM (N = 2). **(c)** EMSAs testing binding to a 150-bp DNA substrate for different RM-TDB constructs. Quantification is in **Fig. 4b**. **(d)** SDS PAGE of purified protein complexes of varying lengths. **(e)** Representative AFM images of 2 μM RM-TDB domain in the absence of DNA. **(f)** Representative AFM images of condensates formed with 1 ng/μl 1000-bp DNA by Rec114$_{388-428}$ complexes with Mei4$_N$. Left, 200 nM protein concentration; right, 1 μM. **(g)** EMSA of Rec114$_C$ alone binding to 1000-bp DNA and its quantification (right). This experiment was conducted once; the apparent K$_d$ is ~300 nM. **(h)** Representative AFM images of 6 μM Rec114$_C$ in the absence (left) or presence (right) of 1.7 ng/μl supercoiled pUC19 plasmid DNA. **(i)** Complexes of Rec114$_C$–Mei4$_N$ (70 nM) bound to 1 ng/μl 1000-bp DNA substrate, categorized by the number and position of the DNA-bound protein particles at either the DNA end or internally (mid). **(j)** Lengths of individual protein-bound DNA segments, grouped according to position at the DNA end (N = 76) or internally (mid, N = 80). Lines represent mean ± SD. **(k)** Comparison of total DNA or protein-DNA volumes in the absence (blue, N = 63) and presence (red, N = 80) of Rec114$_C$–Mei4$_N$. Median and quartiles are indicated by dashed and dotted lines, respectively. The p values in panels j and k are from unpaired two-tailed Student's t-tests.
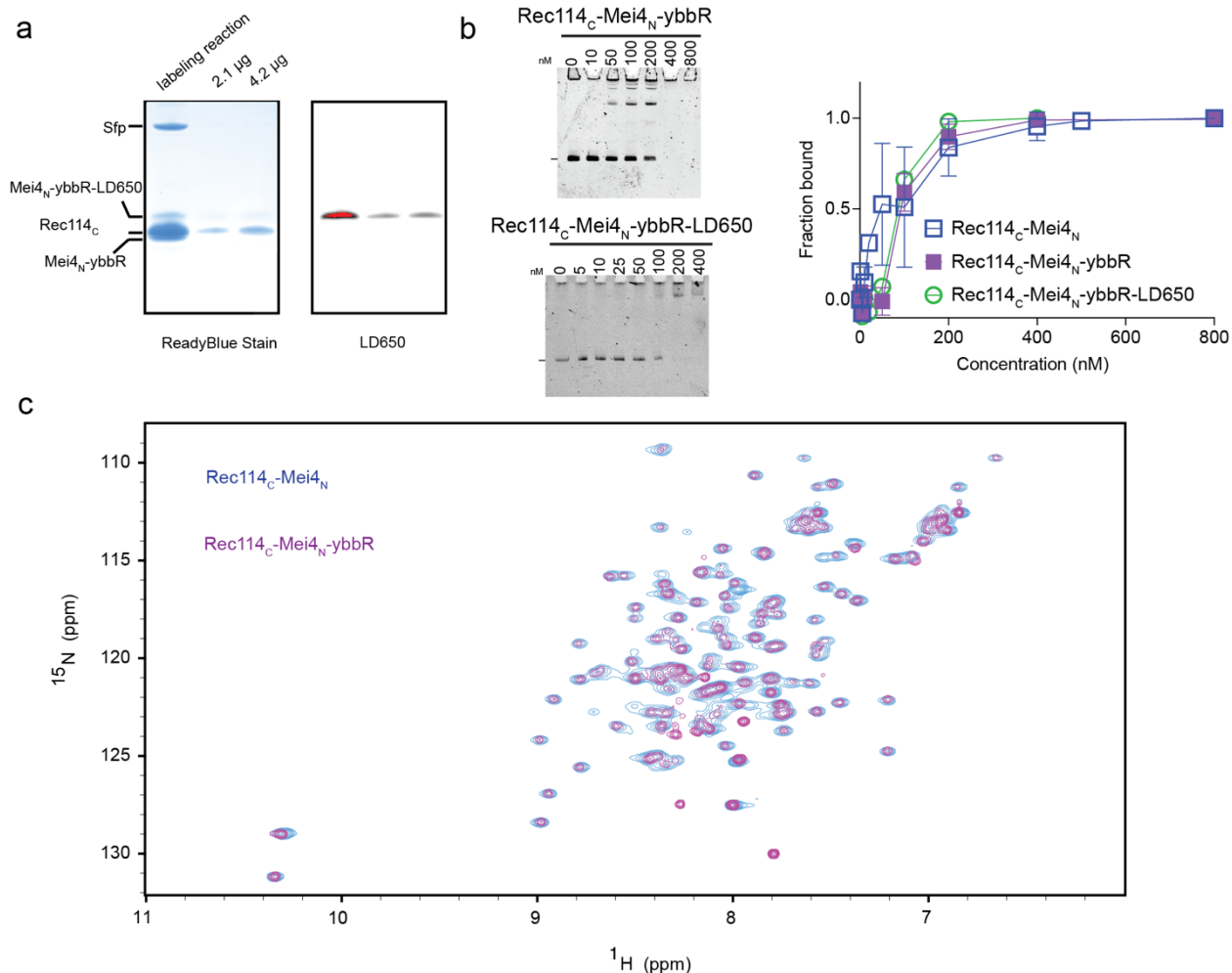
Fig. s8: Fluorescent labeling of the RM-TDB domain. (a) Purified complexes of Rec114$_C$ plus Mei4$_N$-ybbR were covalently labeled with LD650 using Sfp and analyzed by SDS-PAGE followed by ReadyBlue staining (left) or fluorescence scanning (right). After labeling, the sample was further purified by SEC to remove Sfp and unincorporated dye. First lane: labeling reaction; second and third lanes: SEC-purified protein. Mei4-ybbR covalently labeled with LD650 showed a shift to lower mobility. **(b)** EMSA comparing ability of the RM-TDB domain with or without the ybbR tag to bind to a 150-bp DNA substrate; the tagged protein was also tested before and after the fluorescent labeling reaction. Error bars indicate mean ± range for two different experiments with the ybbR-tagged protein (apparent K$_d$ of 90 ± 20 nM), or mean ± SD from three replicates for untagged (reproduced from **Fig. 4b** to aid comparison). The EMSA was conducted once for the labeled protein preparation (apparent K$_d$ of ~90 nM). **(c)** Comparison of the {^{1}H-^{15}N} HSQC spectrum of RM-TDB carrying the unlabeled ybbR tag with that of untagged RM-TDB shows additional signals, likely originating from the ybbR peptide, but otherwise no significant changes.
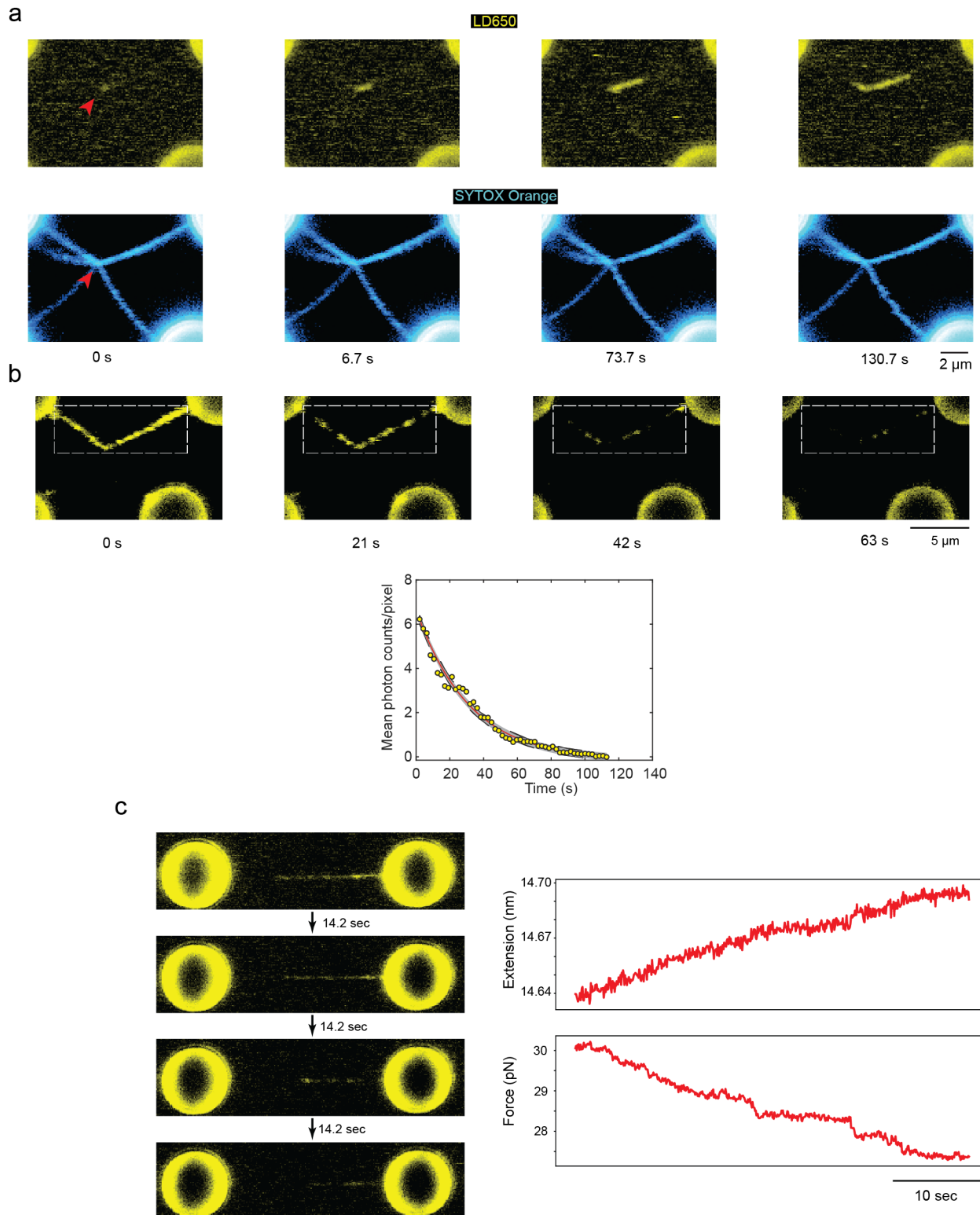
Fig. s9: DNA bridging by the RM-TDB domain. (a) Preferential initiation of RM-TDB binding at a crossing point. A quadruple-trap setup was used to capture two tethered pairs of beads. The top pair is connected by multiple λ DNA tethers, while the bottom pair is connected by only a single DNA. The two sets of tethers were wrapped around each other to form a single crossing

point, then moved into the protein channel to allow RM-TDB to bind. The protein bound initially at or near the crossing point (red arrow), then spread over time to the regions where DNA could be coaligned. **(b)** Reversibility of RM-TDB bridges. To quantify the dissociation rate when beads with preassembled bridge-tether assemblies were moved to the protein-free channel, a region of interest (ROI) was drawn as indicated by the white dashed box for all the frames in the movie. The mean photon count per pixel was then determined for each frame and plotted as a function of time (below). The data was then fit to a single-exponential curve. For this example, the dissociation rate was 0.032 s^{-1} (95% confidence interval: [0.031 s^{-1}, 0.033 s^{-1}]). See also Methods. **(c)** Force-dependent reversal of RM-TDB bridges. In contrast to the experiment shown in **Fig. 5f,** here the optical traps were held in the protein-containing channel at a fixed distance apart that placed an initial force of ~30 pN on a preassembled bridge-tether assembly. Dissociation of the RM-TDB domain was accompanied by an increase in the DNA extension (distance between the beads themselves) and a concomitant decrease of the force.
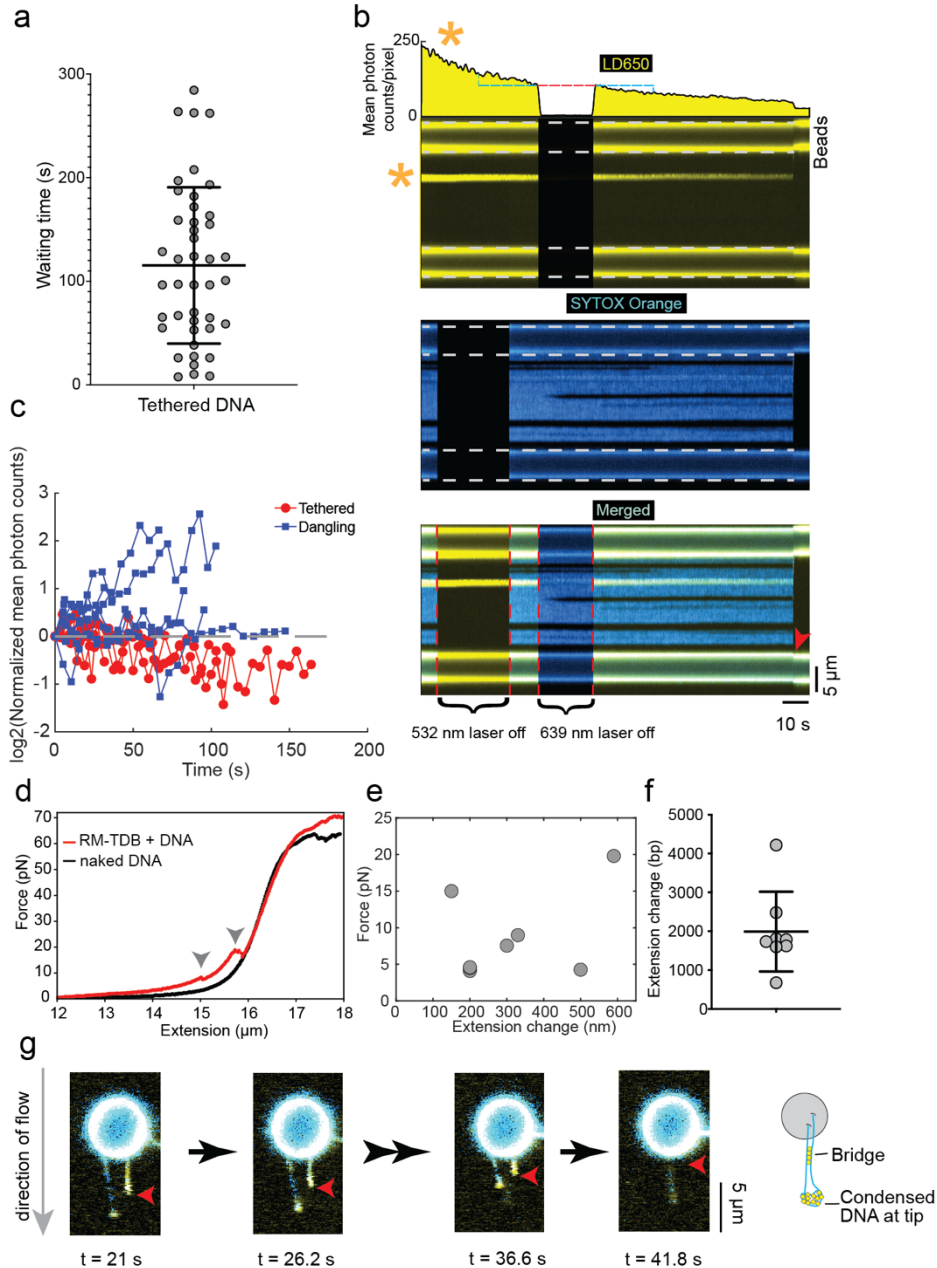
Fig. s10: Characterization of focal DNA binding by the RM-TDB domain. (a) Waiting times for appearance of foci of the RM-TDB domain binding to stretched DNA tethers. Each point shows the time from transfer of the bead-bound DNA into the protein channel to the time when a focal binding event was first detected. Error bars are mean ± SD. **(b)** Kymograph showing a representative RM-TDB focus (asterisk) stably bound to a stretched DNA tether, held in the fluorescent protein-containing channel. The bead boundaries are indicated by white dashed lines. Each laser was turned off briefly to show that there is negligible crosstalk between the DNA and protein fluorescence channels. Double-stranded DNA regions were stained by SYTOX Orange (shown in cyan); the dark regions are single-stranded regions that formed when duplex DNA next to spontaneous nicks was denatured by the 60 pN force applied. The RM-TDB focus remained stably bound to the tether with little or no change in position until the tether broke (indicated by the red arrow at the end). The graph above the image for the LD650 channel

shows the decrease in fluorescence intensity over time for the focal binding event shown in the kymograph. Because each labeled RM-TDB trimer has a single fluorophore, the smooth decay in fluorescence signal without obvious individual steps indicates that many copies of the RM-TDB domain are present in a single focus. The intensity immediately before and after the time when the 639 nm laser was off (red dashed line) was essentially identical. This contrasts with the decrease seen during illumination periods of the same duration (blue dashed lines), therefore the signal decay (~0.01 s^{-1} (range 0.007–0.013 s^{-1}, from fitting before and after 639 nm laser off signal decay)) is primarily due to photo bleaching. **(c)** Change in protein fluorescence intensity over time for focal binding events on stretched tethers (red, N = 4) or on dangling DNA (blue, N = 9). Each trace represents one binding event. These are the individual traces that are averaged in **Fig. 5h**. The protein fluorescence intensity at each time point was normalized to the signal in the first frame where binding of RM-TDB was detected (see Methods). **(d,e,f)** Evidence for force-dependent disruption of long-range interactions between distal DNA segments bound by RM-TDB foci. Panel d compares force-extension curves between naked and protein-bound λ DNA. Arrows indicate examples of abrupt transitions in the curve for protein-bound DNA. Panel e shows the variation of applied force and DNA extension distance for abrupt transitions in force-extension curves from 6 different molecules. Panel f shows the distribution of estimated DNA extension lengths from the transitions in panel e. Lines indicate mean ± SD. The disruption forces ranged from 4–20 pN, with an average disrupted DNA length of ~2000 bp. **(g)** A representative example showing stretches of RM-TDB binding on the coaligned arms of a dangling λ DNA molecule coincident with brighter signal at the tip (red arrow). Over time, the DNA was pulled upward against flow toward the bead surface. A cartoon is provided to aid illustration of the process on the right.
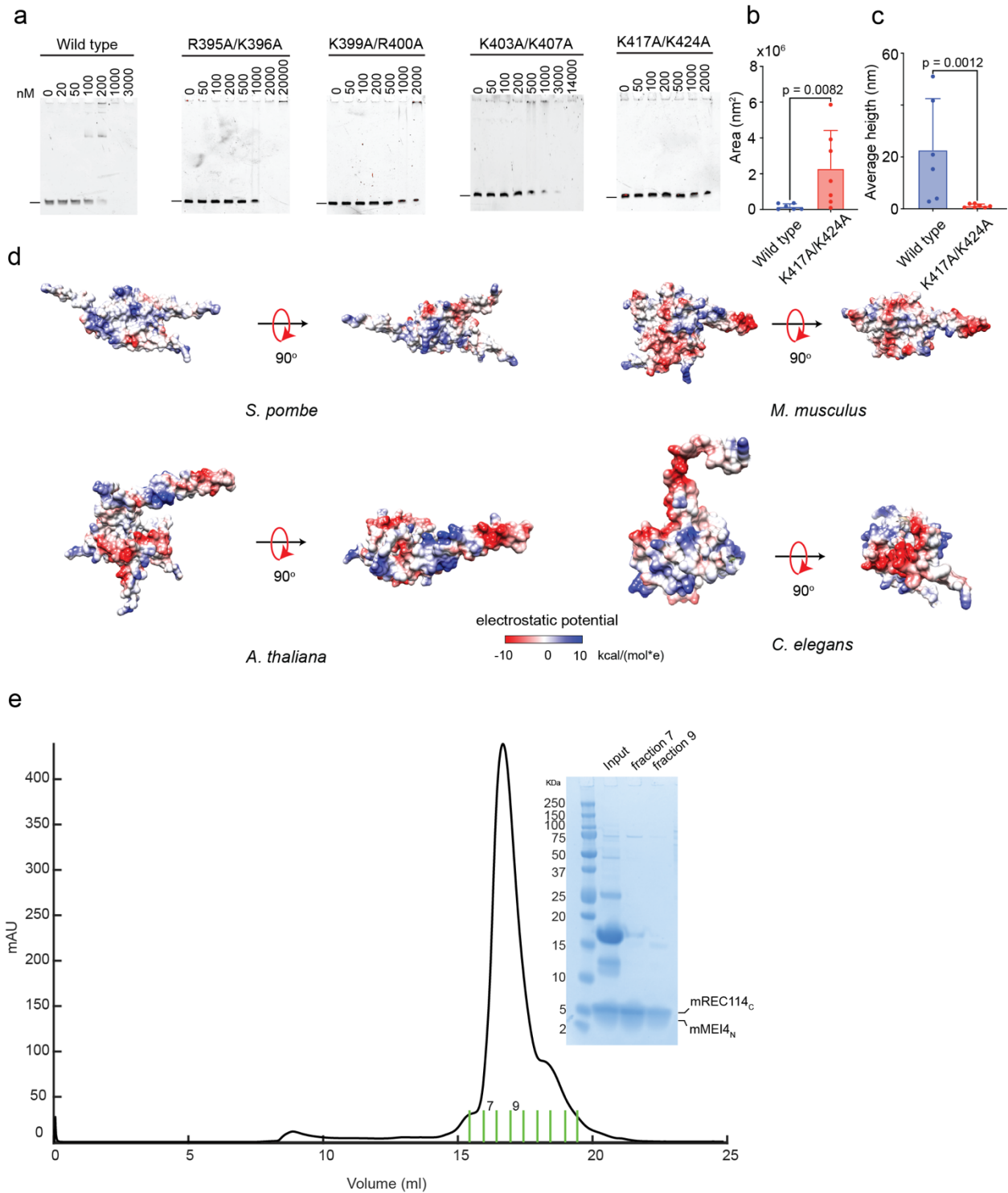
Fig. s11: Conservation and variation of DNA-binding properties of the RM-TDB domain.
(a) Representative EMSAs of wild-type and mutant RM-TDB domains (complexes of $Rec114_{388-428}$ with $Mei4_N$) binding to a 150-bp DNA substrate. Quantification is in **Fig. 6b**. **(b, c)** Comparison of the distributions of areas (panel b) and heights (panel c) of condensates formed by either wild type (N = 6 condensates) or the K417A/K424A mutant (N = 7) measured by AFM as in **Fig. 6c**. Error bars indicate SD. The p values are from two-sided Mann-Whitney tests. **(d)**

Electrostatic surface potentials for orthologous Rec114$_C$–Mei4$_N$ complexes from the indicated species. Views are the same as in **Fig. s6c**. (**e**) SEC purification of mouse RM-TDB domain (mREC114$_C$-MEI4$_N$). The input to the column and fractions 7 and 9 were analyzed by SDS-PAGE and ReadyBlue staining.